# Impedance Reshaping Band Coupling and Broadband Passivity Enhancement for DFIG System

Hu, Bin; Nian, Heng; Li, Haipan; Chen, Liang; Sahoo, Subham; Blaabjerg, Frede

*Published in:*
I E E E Transactions on Power Electronics

*DOI (link to publication from Publisher):*
10.1109/TPEL.2023.3270364

*Publication date:*
2023

*Document Version*
Accepted author manuscript, peer reviewed version

# Impedance Reshaping Band Coupling and Broadband Passivity Enhancement for DFIG System

Bin Hu, *Student Member, IEEE*, Heng Nian, *Senior Member, IEEE*, Haipan Li, Liang Chen, Subham Sahoo, *Senior Member, IEEE*, Frede Blaabjerg, *Fellow, IEEE*

***Abstract*—Doubly fed induction generator (DFIG)-based wind power systems incur a broadband negative resistive characteristic, resulting in resonance risks when connected with weak grid or diverse grid transmission infrastructure. The dominant factor and underlying mechanism of this broadband negative resistive characteristic are analyzed based on the passivity-based stability assessment. It is then noticed that the negative resistive region within low frequency, middle frequency and high frequency are closely linked to the current controller, phase locked loop and system delay, respectively. This article reveals the impedance reshaping band coupling phenomenon to facilitate some passivity-based designs, then puts forward a broadband passivity enhancement method for DFIG system. The experimental results validate the aforementioned conclusions and the effectiveness of the proposed passivity enhancement method.**

***Index Terms*— Doubly-fed induction generator, negative resistive characteristic, phase locked loop, broadband passivity enhancement method.**

## I. Introduction

Over the past decades, the fossil fuels are gradually being replaced by the high penetration renewable energy sources to bring down $CO_2$ emissions [1], wherein the installed capacity of wind farms has experienced fast growth [2]. Since the numerous wind energy conversion system are concentrated in remote areas, the grid impedance is non-negligible and the power grid is becoming weaker [3]-[5]. Moreover, the grid includes grid transmission infrastructure such as reactive power compensation, long transmission cables and high-voltage direct current (HVDC) system, resulting in a complex grid network [6].

It has been reported that when connected with low short circuit ratio (SCR) grid or diverse grid transmission infrastructure, the doubly fed induction generator (DFIG)-based wind power systems have some resonance risk, wherein the range of resonance frequency is very wide [7]. For instance, [8]-[10] analyze the sub-synchronous resonance (SSR) at low frequency, which has been detected in series-compensated power networks of Texas, USA and Hebei, China. According to [11]-[13], some resonance issues around fundamental frequency are investigated in the Horn offshore wind farm, accompanied by the frequency coupling phenomenon for an asymmetrical controller, that is commonly known as sub/super-synchronous oscillation (SSO). The high-frequency resonance (HFR) of DFIG system always occurs under the condition of parallel-compensated grid or long transmission cable. The authors of [14] and [15] also investigate the cause of this HFR.

In view of the impedance-based stability analysis, the mechanism of these resonance issues is that DFIG system possesses the broadband negative resistive characteristics [7], [11]. In other words, the phase of DFIG system will exceed ±90°, leading to a phase difference greater than 180° of the interconnected system.

The passivity-based assessment has recently emerged as a promising way to tackle these instability challenges [15]-[18]. If the real part of the impedance is non-negative for the whole frequency band, the critical grid resonance will always fall within regions where the phase margin is sufficient [15]. In this scenario, the destabilization is generally prevented regardless of converter number or grid structure [16]. Substantial research efforts have been devoted to the passivity-based stability assessment, e.g., grid-connected voltage-source converter (VSC) [17], modular multilevel converters (MMCs) [15] and line-commutated converter (LCC)-based HVDC [18]. Nevertheless, the stator of DFIG, comprising the generator characteristics, which is directly connected to the grid, complicates the passivity-based stability assessment [12].

Recently, there are many impedance reshaping methods to pave the way for passivity enhancement. At low frequency, the adaptive damping control [8] and sub-synchronous notch filter [9] are two feasible approaches. Around fundamental frequency, [7] and [12] propose the direct power control (DPC) and reference calculation matrix. At high frequency, the variable frequency resistance and virtual-flux-based control are recommended in [14] and [15]. Actually, these passivity-based design methodologies usually pay attention on the oscillating frequency band. As for the DFIG system with broadband negative resistive region, these passivity-based design approaches may have the impedance reshaping band coupling, such that the impedance characteristics of other frequency bands will change after adding these impedance reshaping controller, and then lead to some new stability problems when the grid parameters vary.

Overall, this article addresses the following three questions of the broadband passivity enhancement for DFIG system:

1) The main reason for deviating passive region is due to some controllers [7], i.e. current controller or phase locked loop

This work was supported by the National Natural Science Foundation of China under Grant 51977194. *(Corresponding author: Heng Nian.)*

B. Hu, H. Nian and H. Li are with the College of Electrical Engineering, Zhejiang University, Hangzhou, China (e-mail: 11810031@zju.edu.cn; lihaipan@zju.edu.cn; nianheng@zju.edu.cn).

L. Chen is with the School of Information Science and Engineering, NingboTech University, Ningbo, China (e-mail: 21410077@zju.edu.cn).

S. Sahoo and F. Blaabjerg are with the Department of Energy, Aalborg University, Aalborg, Denmark. (email: sssa@energy.aau.dk; fbl@energy.aau.dk).

(PLL). What is the impact on impedance characteristics when considering these controllers?

2) Since the negative resistive region of DFIG system is very wide [7]. How to divide each frequency band for DFIG system? What is the dominant factor and underlying mechanism of each frequency band?

3) The resonance issue around fundamental frequency is within the controller bandwidth, which is more complicated than SSR and HFR. This requires an analysis of whether some impedance reshaping controllers near fundamental frequency, will deteriorate the low-frequency or high-frequency stability?

The rest of this article is organized as follows. Section II describes the topology and impedance model of DFIG system connected with weak grid. Section III analyzes the broadband negative resistive characteristics when considering control. The dominant reason and underlying mechanism of negative resistive characteristics within each frequency band are revealed in Section IV. Then the impedance reshaping band coupling and broadband passivity enhancement are studied in Section V. Section VI conducts the experiments and Section VII summarizes the conclusions.

## II. Topology and Impedance Model of DFIG System Connected with Weak Grid

### A. Investigated Configuration of DFIG System

The control signals of DFIG system are generated by the grid side converter (GSC) and the rotor side converter (RSC), which keeps the stable dc voltage and achieves the maximum power point tracking (MPPT), respectively.

Though there are some articles highlighting the coupling effects of RSC and GSC via the dc capacitor, [19] also analyzes that this dc-link dynamic can be ignored when utilizing the compensated modulation or larger dc-bus capacitance. And it is widely accepted that the DFIG+RSC plays a leading role in introducing negative resistive characteristics [11]. The reason lies in the fact that: 1) The overall DFIG system impedance is equal to the parallel connection of GSC and DFIG+RSC, thereby the one with smaller magnitude being more dominant; 2) the magnitude of impedance is related to the output power within controller bandwidth, but GSC can only provide limited slip power; 3) the filter inductor between the GSC and the point of common coupling (PCC) is larger than the leakage inductor of DFIG system, which further increases the magnitude of GSC at high frequency.

The same conclusion that the GSC can be ignored when analyzing the origin of negative resistance has been proposed in [7], [13]. Therefore, the passivity enhancement for DFIG+RSC is more effective to enhance the stability of DFIG system. The investigated configuration diagram connected with weak grid is depicted in Fig. 1.

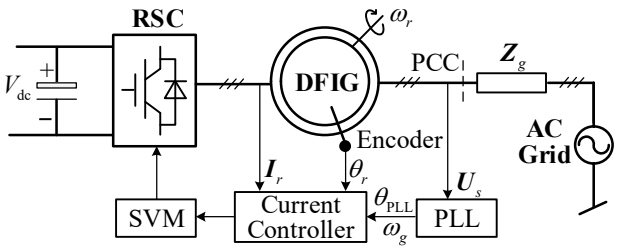


Fig. 1. Investigated configuration of DFIG+RSC connected with AC grid.

In Fig. 1, the bold variables denote the complex space vector or 2×2 matrix in this article. $U$ and $I$ denote the voltage and current. The subscripts $s$ and $r$ represent the stator and rotor parameters. The dc-link voltage $V_{dc}$ is assumed to be constant. $\boldsymbol{Z}_g$ is the grid impedance. The stator voltage $\boldsymbol{U}_s$ and rotor current $\boldsymbol{I}_r$ are sampled from PCC and DFIG rotor, respectively. The grid angle $\theta_{PLL}$ and the grid angular frequency $\omega_g$ are obtained by the PLL. The rotor angle $\theta_r$ and the rotor angular frequency $\omega_r$ are obtained by the encoder. The drive signals are generated by the current controller and the space vector modulation (SVM).

### B. Impedance Model Ignoring or Considering Control

According to [7], the sequence-impedance model of DFIG system ignoring or considering control are depicted in Fig. 2, of which the detailed admittance expressions $1/\boldsymbol{Z}_{DM}$ and $1/\boldsymbol{Z}_{DFIG}$ are shown in (1) and (2).

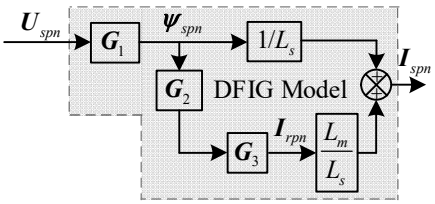


(a) $1/\boldsymbol{Z}_{DM}$ (Ignore control)

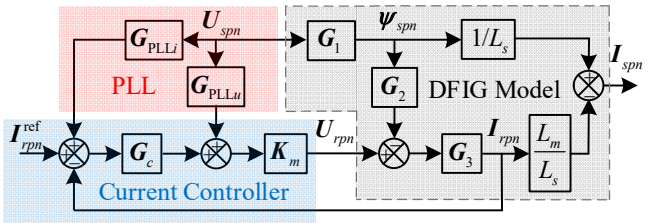


(b) $1/\boldsymbol{Z}_{DFIG}$ (Consider control)

Fig. 2. Impedance model of DFIG system ignoring or considering control.

$$1/\boldsymbol{Z}_{DM}=\frac{\boldsymbol{I}_{spn}}{\boldsymbol{U}_{spn}}=\frac{1}{L_s}\boldsymbol{G}_1+\frac{L_m}{L_s}\boldsymbol{G}_3\boldsymbol{G}_2\boldsymbol{G}_1 \tag{1}$$

$$1/\boldsymbol{Z}_{DFIG}=\frac{\boldsymbol{I}_{spn}}{\boldsymbol{U}_{spn}}=\frac{1}{L_s}\boldsymbol{G}_1-\frac{L_m\boldsymbol{G}_3\left(\boldsymbol{K}_m\boldsymbol{G}_{PLLu}+\boldsymbol{K}_m\boldsymbol{G}_c\boldsymbol{G}_{PLLi}-\boldsymbol{G}_2\boldsymbol{G}_1\right)}{L_s\left(\boldsymbol{I}+\boldsymbol{K}_m\boldsymbol{G}_c\boldsymbol{G}_3\right)} \tag{2}$$

The existence of PLL and current controller further complicate the impedance characteristics. Where $\boldsymbol{G}_1$, $\boldsymbol{G}_2$ and $\boldsymbol{G}_3$ are related to the DFIG parameters. $\boldsymbol{G}_c$ and $\boldsymbol{K}_m$ are related to the current controller and the system delay, respectively. Since there are some small-signal perturbations in the PLL angle $\theta_{PLL}$ [12], two PLL matrices $\boldsymbol{G}_{PLLi}$ and $\boldsymbol{G}_{PLLu}$ are introduced. $\boldsymbol{G}_{PLLi}$ is related to the Park transformation of rotor current. $\boldsymbol{G}_{PLLu}$ is related to the

inverse Park transformation of rotor voltage. The subscripts $p$ and $n$ denote the positive and negative sequence components. The superscript ref denotes the reference value. $\Psi$ is the flux linkage. $L_s$=$L_{ls}$+$L_m$ and $L_r$=$L_{lr}$+$L_m$ are the self-inductance of stator and rotor windings. $L_{ls}$, $L_{lr}$, $L_m$ are the stator leakage inductance, rotor leakage inductance and mutual inductance. The detailed expressions of matrices $\boldsymbol{G}_1$, $\boldsymbol{G}_2$, $\boldsymbol{G}_3$, $\boldsymbol{G}_c$, $\boldsymbol{K}_m$, $\boldsymbol{G}_{\mathrm{PLL}i}$ and $\boldsymbol{G}_{\mathrm{PLL}u}$ are as,

$$\boldsymbol{G}_1=\begin{bmatrix}\frac{1}{s} & 0\\ 0 & \frac{1}{s-2j\omega_g}\end{bmatrix}\quad \boldsymbol{G}_2=\frac{L_m}{L_s}\begin{bmatrix}s-j\omega_r & 0\\ 0 & s+j\omega_r-2j\omega_g\end{bmatrix}$$

$$\boldsymbol{G}_3=\begin{bmatrix}\frac{1}{R_r+(s-j\omega_r)L_r\sigma} & 0\\ 0 & \frac{1}{R_r+(s+j\omega_r-2j\omega_g)L_r\sigma}\end{bmatrix} \tag{3}$$

$$\boldsymbol{G}_c=\begin{bmatrix}K_{pc}+K_{ic}/(s-j\omega_g) & 0\\ 0 & K_{pc}+K_{ic}/(s-j\omega_g)\end{bmatrix} \tag{4}$$

$$\boldsymbol{K}_m=\begin{bmatrix}e^{-1.5s/f_s} & 0\\ 0 & e^{-1.5(s-2j\omega_g)/f_s}\end{bmatrix} \tag{5}$$

$$\boldsymbol{G}_{\mathrm{PLL}i}=\underbrace{\frac{1}{2}H_{\mathrm{PLL}}(s)\begin{bmatrix}\boldsymbol{I}_{rdq0} & -\boldsymbol{I}_{rdq0}\\ -\boldsymbol{I}^*_{rdq0} & \boldsymbol{I}^*_{rdq0}\end{bmatrix}}_{\text{SRF-PLL}}\Rightarrow\underbrace{H_{\mathrm{PLL}}(s)\begin{bmatrix}\boldsymbol{I}_{rdq0} & 0\\ 0 & \boldsymbol{I}^*_{rdq0}\end{bmatrix}}_{\text{Symmetrical PLL}} \tag{6}$$

$$\boldsymbol{G}_{\mathrm{PLL}u}=\underbrace{\frac{1}{2}H_{\mathrm{PLL}}(s)\begin{bmatrix}\boldsymbol{U}_{rdq0} & -\boldsymbol{U}_{rdq0}\\ -\boldsymbol{U}^*_{rdq0} & \boldsymbol{U}^*_{rdq0}\end{bmatrix}}_{\text{SRF-PLL}}\Rightarrow\underbrace{H_{\mathrm{PLL}}(s)\begin{bmatrix}\boldsymbol{U}_{rdq0} & 0\\ 0 & \boldsymbol{U}^*_{rdq0}\end{bmatrix}}_{\text{Symmetrical PLL}} \tag{7}$$

where $R_r$ is the rotor resistance. $\sigma$=1-$L_m^2$/($L_s$·$L_r$). $K_{pc}$ and $K_{ic}$ are the proportional integral (PI) gains of current controller. The delay time is equal to 1.5 times the switching period 1/$f_s$. $H_{\mathrm{PLL}}(s)$=$H_p(s)$/[$U_{sd0}H_p(s)$+$s$-$j\omega_g$]. The subscripts $d$ and $q$ represent the components in the synchronous reference frame. The steady-state component is represented as subscript 0. * denotes the conjugate operator. The PI controller of the PLL is denoted as $H_p(s)$=$K_{pp}$+$K_{ip}$/($s$-$j\omega_g$), in which $K_{pp}$ and $K_{ip}$ are the PI gains of PLL.

## III. Broadband Negative Resistive Characteristic when Considering Control

It is worth notifying that the positive-sequence impedance is sufficient to describe the impedance characteristics when there is no frequency coupling [3]. According to (1), the DFIG system impedance $Z_{\mathrm{DM11}}$ which ignores the controller is depicted below:

$$Z_{\mathrm{DM11}}(s)=\frac{sL_s^2\left[R_r+(s-j\omega_r)L_r\sigma\right]}{(s-j\omega_r)L_sL_r\sigma+L_sR_r+(s-j\omega_r)L_m^2} \tag{8}$$

The subscript "11" in $Z_{\mathrm{DM11}}$ denotes the first element in the first row of the matrix, which represents the positive-sequence impedance. Compared with $(s\text{-}j\omega_r)L_m^2$ in the denominator, $(s\text{-}j\omega_r)L_sL_r\sigma$ and $L_sR_r$ are much smaller, which can be neglected to give:

$$Z_{\mathrm{DM11}}(s)\approx\frac{sL_s^2\left[R_r+(s-j\omega_r)L_r\sigma\right]}{(s-j\omega_r)L_m^2} \tag{9}$$

Substituting '$s$=$j\omega$' into (9), the real part of $Z_{\mathrm{DM11}}(s)$, i.e. $\mathrm{Re}\{Z_{\mathrm{DM11}}(j\omega)\}$ can be obtained as:

$$\mathrm{Re}\{Z_{\mathrm{DM11}}(j\omega)\}\approx\frac{\omega L_s^2R_r}{(\omega-\omega_r)L_m^2} \tag{10}$$

It can be found that $Z_{\mathrm{DM11}}$ behaves as a negative resistor when $\omega$ is less than the rotor angular frequency $\omega_r$, which is called as the induction generator effect (IGE) [10].

TABLE I
PARAMETERS OF DFIG SYSTEM

| Parameter | Value | Parameter | Value |
|---|---|---|---|
| $U_s$, Rated Voltage | 690 V | $R_s$, Stator resistance | 2.4 mΩ |
| $P_s$, Rated power | 1.5 MW | $R_r$, Rotor resistance | 2 mΩ |
| $f_g$, Fundamental frequency | 50 Hz | $L_{ls}$, Stator leakage | 0.06 mH |
| $f_r$, Rotor frequency | 35 Hz | $L_{lr}$, Rotor leakage | 0.083 mH |
| $n_p$, Pole pairs | 2 | $L_m$, Mutual inductance | 4.43 mΩ |
| $K_e$, Turns ratio | 0.33 | $f_s$, Switching frequency | 5 kHz |
| $V_{\mathrm{dc}}$, Dc-link voltage | 1050 V | | |

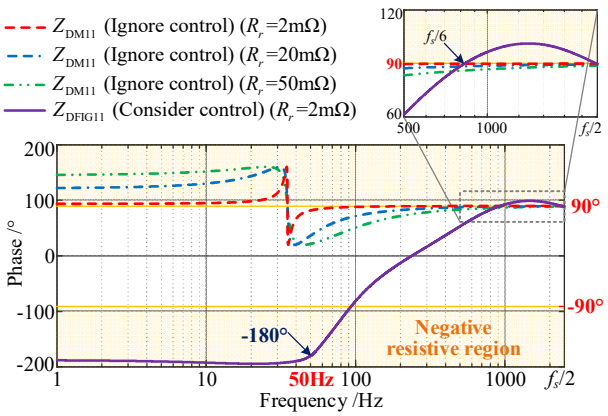


Fig. 3. Phase-frequency characteristic curves of DFIG system ignoring or considering control.

Fig. 3 depicts the phase-frequency characteristic curves of the DFIG system, with the DFIG system parameters shown in Table I. The negative resistive characteristics of $Z_{\mathrm{DM11}}$ will be more obvious with the increment of rotor resistor $R_r$. However, $R_r$ will not be too large for a megawatt DFIG-based wind energy conversion [10]. As for $R_r$=2 mΩ, this negative resistive characteristic only exists around the rotor angular frequency, i.e. $f$=35 Hz. It verifies that there is not many SSR caused by induction generator effect (IGE-type SSR) in practice.

According to (2), Fig. 3 also depicts the positive-sequence DFIG system impedance $Z_{\mathrm{DFIG11}}$ considering control. The proportional gain $K_{pp}$ and integral gain $K_{ip}$ of PLL are 1 and 10 (PLL bandwidth $f_{bw\_PLL}$=90 Hz). The proportional gain $K_{pc}$ and integral gain $K_{ic}$ of current controller are 0.19 and 19 (Current controller bandwidth $f_{bw\_CC}$=210 Hz). Since the PLL matrices

$\boldsymbol{G}_{\mathrm{PLL}i}$ and $\boldsymbol{G}_{\mathrm{PLL}u}$ have four elements for synchronous reference frame (SRF) PLL, this article employs symmetrical PLL, which controls both *d*- and *q*-axis voltage to remove frequency coupling as shown in (6) and (7) [11]. Note that the symmetrical PLL is just a way to simplify the impedance analysis. In fact, the following negative resistive characteristics analysis and the stability enhancement methods are also applicable to the traditional SRF-PLL [7]. Then, it is noticed that after considering control, the broadband phase of DFIG system lies in the negative resistive region even though $R_r$=2 mΩ. Fig. 3 also gives an enlarged view at high frequency, where the phase from $f_s$/6 to $f_s$/2 Hz is over 90°. In summary, it is necessary to analyze the cause of broadband negative resistive characteristic after considering control, and propose some passivity enhancement methods.

## IV. Impedance-Based Analysis of Negative Resistive Characteristic within Broadband Frequency

### A. Dominant Reason of Each Frequency Band

Since this negative resistive region is very wide, it is required to find the dominant reason of each frequency band.

According to Fig. 2 (b) and superposition theorem, the impedance model of DFIG system can be categorized into two parts as shown in Fig. 4, i.e. $1/\boldsymbol{Z}_{\mathrm{DFIG}}=1/\boldsymbol{Z}_{\mathrm{PLL\_CC}}+1/\boldsymbol{Z}_{\mathrm{DM\_CC}}$. where $\boldsymbol{Z}_{\mathrm{PLL\_CC}}$ mainly consists of PLL and current controller, $\boldsymbol{Z}_{\mathrm{DM\_CC}}$ is the original DFIG model embedded in the current controller. The detailed admittance expressions are shown in (11) and (12). Note that the $\boldsymbol{G}_c$ appears in both subsystem impedances.

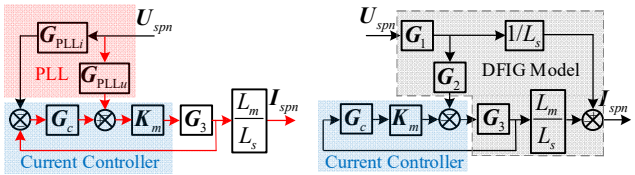


(a) $1/\boldsymbol{Z}_{\mathrm{PLL\_CC}}$ (b) $1/\boldsymbol{Z}_{\mathrm{DM\_CC}}$

Fig. 4. Impedance subsystem of DFIG system considering control.

$$1/\boldsymbol{Z}_{\mathrm{PLL\_CC}}=\frac{\boldsymbol{I}_{spn}}{\boldsymbol{U}_{spn}}=-\frac{L_m\boldsymbol{G}_3\left(\boldsymbol{K}_m\boldsymbol{G}_{\mathrm{PLL}u}+\boldsymbol{K}_m\boldsymbol{G}_c\boldsymbol{G}_{\mathrm{PLL}i}\right)}{L_s\left(\boldsymbol{I}+\boldsymbol{K}_m\boldsymbol{G}_c\boldsymbol{G}_3\right)} \tag{11}$$

$$1/\boldsymbol{Z}_{\mathrm{DM\_CC}}=\frac{\boldsymbol{I}_{spn}}{\boldsymbol{U}_{spn}}=\frac{1}{L_s}\boldsymbol{G}_1+\frac{L_m\boldsymbol{G}_3\boldsymbol{G}_2\boldsymbol{G}_1}{L_s\left(\boldsymbol{I}+\boldsymbol{K}_m\boldsymbol{G}_c\boldsymbol{G}_3\right)} \tag{12}$$

Fig. 5 depicts the amplitude-frequency characteristic curves of positive-sequence impedance for (2), (11) and (12). The $Z_{\mathrm{DM\_CC11}}$ dominates the impedance characteristics from 1 to 10 Hz and 200 to $f_s$/2 Hz. This is because the PLL possesses limited bandwidth, and has little impact on these frequency bands. Yet, $Z_{\mathrm{DM\_CC11}}$ and $Z_{\mathrm{PLL\_CC11}}$ together determine the impedance characteristics from 10 to 200 Hz. To this end, the DFIG system impedance can be classified into three frequency bands to analyze the cause of negative resistive characteristic specifically, i.e. low frequency (1 to 10 Hz), middle frequency (10 to 200 Hz) and high frequency (200 to $f_s$/2 Hz).

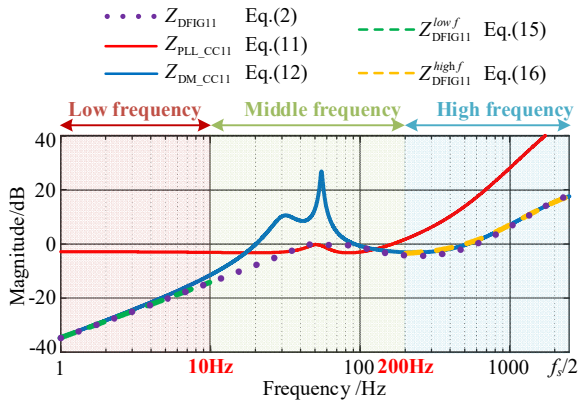


Fig. 5. Amplitude-frequency characteristic curves of DFIG system considering control.

### B. Cause of Negative Resistive Characteristic at Low and High Frequency Band

Since the leakage inductance $L_{ls}$ and $L_{lr}$ are small, $L_s$ and $L_r$ can be approximate to $L_m$. As mentioned in Section III that IGE-type SSR rarely appears in reality, $R_r$ can be eliminated to acquire a simpler impedance expression.

The DFIG system is dominated by $Z_{\mathrm{DM\_CC11}}$ at low and high frequency, such the detailed $Z_{\mathrm{DM\_CC11}}$ is given by:

$$Z_{\mathrm{DM\_CC11}}(s)=\frac{sL_m\left[(s-j\omega_g)(s-j\omega_r)L_m\sigma+G_x(s)\right]}{(s-j\omega_g)(s-j\omega_r)L_m(1+\sigma)+G_x(s)} \tag{13}$$

$$G_x(s)=e^{-1.5s/f_s}\left[K_{pc}(s-j\omega_g)+K_{ic}\right] \tag{14}$$

where $(1+\sigma)$ in the denominator can be assumed to 1 due to $\sigma$=0.0315 in this article. At low frequency ($f$<10 Hz), the system delay is ignored, then assuming $(s\text{-}j\omega_g)\approx\text{-}j\omega_g$ and $(s\text{-}j\omega_r)\approx\text{-}j\omega_r$. The simplified low-frequency impedance model is expressed as:

$$Z_{\mathrm{DFIG11}}(s)\overset{low\,f}{\approx}\frac{s\omega_g\omega_rL_m{}^2\sigma+sL_m\left(jK_{pc}\omega_g-K_{ic}\right)}{\omega_g\omega_rL_m-K_{ic}+jK_{pc}\omega_g} \tag{15}$$

At high frequency ($f$ >200 Hz), the current controller will degenerate into a proportional gain $K_{pc}$ [15], then assuming $(s\text{-}j\omega_g)\approx s$ and $(s\text{-}j\omega_r)\approx s$. The simplified high-frequency impedance model is expressed as,

$$Z_{\mathrm{DFIG11}}(s)\overset{high\,f}{\approx}\frac{s^2L_m{}^2\sigma+sL_mK_{pc}e^{-1.5s/f_s}}{sL_m+K_{pc}e^{-1.5s/f_s}} \tag{16}$$

Fig. 5 also depicts the amplitude-frequency characteristic curves of (15) and (16), which matches the detailed impedance model of (2) well.

Substituting '$s$=$j\omega$' into (15) and (16), the real part can be obtained as,

$$\mathrm{Re}\left\{Z_{\mathrm{DFIG11}}(j\omega)\right\}\overset{low\,f}{\approx}\frac{-\omega\omega_g{}^2\omega_rL_m{}^2(1-\sigma)K_{pc}}{\left(K_{ic}-\omega_g\omega_rL_m\right)^2+\left(K_{pc}\omega_g\right)^2} \tag{17}$$

$$\mathrm{Re}\left\{Z_{\mathrm{DFIG11}}(j\omega)\right\}\overset{high\,f}{\approx}\frac{\omega^2L_m{}^2(1-\sigma)K_{pc}\cos(1.5\omega/f_s)}{\left(\omega L_m-K_{pc}\right)^2+2\omega L_mK_{pc}\left[1-\sin(1.5\omega/f_s)\right]} \tag{18}$$

According to (17), the proportional gain $K_{pc}$ of current controller exhibits the negative resistive characteristic at low frequency. This phenomenon is called the sub-synchronous control interaction (SSCI) [9], which is the main cause of SSR.

Since the denominator of (18) is always larger than zero, the sign of $\mathrm{Re}\{Z_{\mathrm{DFIG11}}(j\omega)\}$ is determined by the numerator. The frequency range of the negative-real-part region can be obtained by solving $\cos(1.5\omega/f_s)<0$, which leads to $f_{\mathrm{neg\_real}}\in(f_s/6, f_s/2)$. Thus, the high-frequency negative resistive characteristic as shown in Fig. 3 is due to the system delay.

### C. Cause of Negative Resistive Characteristic within Middle Frequency Band

The DFIG system within middle frequency is also related to $Z_{\mathrm{PLL\_CC11}}$, while the inverse Park transformation has less impact on impedance characteristics than Park transformation [11]. The reason is given below

Firstly, the red path in Fig. 4 (a) is the transfer function of inverse Park transformation, and the detailed expression can be given by:

$$Y_{\mathrm{PLL}u}(s)=-L_m G_{\mathrm{PLL}u}(s)K_m(s)G_3(s)/\left[L_s+L_sK_mG_3(s)G_c(s)\right]$$
$$=\frac{-L_mH_{PLL}(s)K_m(s)\boldsymbol{U}_{rdq0}(s-j\omega_g)}{(s+j\omega_r-2j\omega_g)(s-j\omega_g)L_sL_r\sigma+L_sK_m(s)[K_{pc}(s-j\omega_g)+K_{ic}]} \tag{19}$$

According to (19), there is a zero point at 50 Hz, indicating that the inverse Park transformation has little gain around fundamental frequency. Nevertheless, the transfer function of Park transformation contains the current controller matrix $\boldsymbol{G}_c$, which cancels out this zero point.

Secondly, the PLL matrix $\boldsymbol{G}_{\mathrm{PLL}u}$ includes the operating point of rotor voltage. When the slip is zero, the rotor voltage is zero too, then the inverse Park transformation will not influence the impedance characteristics. This conclusion also explains the difference between conventional grid-tied inverter and DFIG system, elaborated both the Park and inverse Park transformation have a significant effect for conventional grid-tied inverter [3].

At middle frequency (10 Hz< $f$ <200 Hz), ignoring the inverse Park transformation and the system delay, the simplified middle-frequency impedance model is given by:

$$1/Z_{\mathrm{DFIG11}}(s)\overset{middle\ f}{\approx}\frac{1}{L_ss}+\frac{s\boldsymbol{I}_{rdq0}H_{PLL}(s)G_y(s)+G_z(s)}{s\left[G_y(s)+G_z(s)L_r\sigma\right]} \tag{20}$$

$$G_y(s)=K_{pc}(s-j\omega_g)+K_{ic} \tag{21}$$

$$G_z(s)=(s-j\omega_r)(s-j\omega_g) \tag{22}$$

Substituting '$s=j\omega_g$' into (20), the DFIG system admittance expression at 50 Hz can be obtained as follows:

$$1/Z_{\mathrm{DFIG11}}(j\omega_g)=\frac{1}{j\omega_gL_s}+\frac{\boldsymbol{I}_{rdq0}}{U_{sd0}} \tag{23}$$

The relationships between stator and rotor current are as follows:

$$\begin{cases} I_{rd0}=-\dfrac{L_s}{L_m}I_{sd0} \\ I_{rq0}=-\dfrac{L_s}{L_m}(I_{sq0}+\dfrac{U_{sd0}}{\omega_gL_s}) \end{cases} \tag{24}$$

After combining (23) and (24), the DFIG system with unity power factor ($I_{sq0}$=0) is shown as:

$$Z_{\mathrm{DFIG11}}(j\omega_g)=-\frac{U_{sd0}}{I_{sd0}} \tag{25}$$

It is worth notifying that the phase of DFIG system is always -180° at 50 Hz. This validates with the participation of Park transformation, there will be an obvious negative resistive characteristic within middle frequency as shown in Fig. 3, and the phase starts to rise when the frequency exceeds 50 Hz.

Compared with the existing state-of-art, the abovementioned middle-frequency negative resistive characteristic of DFIG system is first revealed in this article, while the causes of negative resistive characteristic at low and high frequency band are similar to [20] and [15]. But [20] utilizes the equivalent circuit to analyze the low-frequency resonance, which is difficult to transplant to middle-frequency resonance. The contribution of Section IV is to propose a unified form to express all the negative resistive mechanism, such as (10), (15), (16), (20). This unified form is also beneficial the following analysis of reshaping band coupling of DFIG system.

## V. Analysis of Impedance Reshaping Band Coupling

According to Section I, the most popular norm for passivity enhancement is to carry out some impedance reshaping controllers. However, the design of impedance reshaping method within middle frequency is more difficult than low or high frequency, due to the presence of PLL and its proximity to fundamental frequency [11].

### A. DPC for Improving Middle-Frequency Stability

In terms of Section IV.C, the phase of DFIG system at 50 Hz is restricted to -180° because of the Park transformation, which brings significant negative resistive characteristics. Since the active and reactive power are scalars that can be calculated in the stationary frame instead of utilizing the Park transformation [21], the DPC is one of the simplest approaches in achieving passivity enhancement for DFIG system within middle frequency [7]. The impedance model of DFIG system based on DPC is depicted in Fig. 6 [7]. Where $\boldsymbol{G}_{PQu}$ and $\boldsymbol{G}_{PQi}$ are related to the power calculation. $\boldsymbol{S}_s=P_s-jQ_s$ is the complex power.

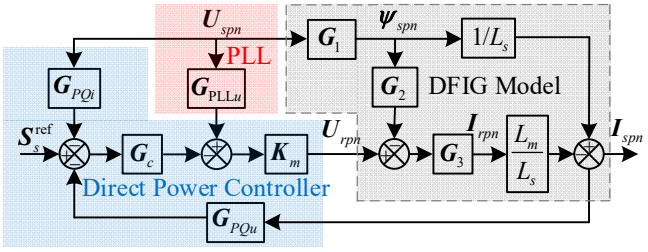


Fig. 6. Impedance model of DFIG system based on DPC.

$$\boldsymbol{G}_{PQu}=\begin{bmatrix}\boldsymbol{U}_{sdq0} & 0\\ 0 & \boldsymbol{U}^{*}_{sdq0}\end{bmatrix}\quad \boldsymbol{G}_{PQi}=\begin{bmatrix}0 & \boldsymbol{I}_{sdq0}\\ \boldsymbol{I}^{*}_{sdq0} & 0\end{bmatrix} \tag{26}$$

According to Fig. 6, the detailed impedance expressions for DPC are shown in (27). The same as Section IV. B, (27) defines $L_s \approx L_r \approx L_m$, $R_r \approx 0$ and $\boldsymbol{K}_m=1$ for simplification.

$$\begin{cases} Z_{\mathrm{DPC11}} \overset{middle\,f}{\approx} \dfrac{(s-j\omega_r)(s-j\omega_g)L_m\sigma+\boldsymbol{U}_{sdq0}[K_{pc}(s-j\omega_g)+K_{ic}]}{(s-j\omega_r)(s-j\omega_g)\left(\dfrac{\sigma+1}{s}\right)} \\ Z_{\mathrm{DPC12}} \overset{middle\,f}{\approx} \dfrac{(s-j\omega_r)(s-j\omega_g)L_m\sigma+\boldsymbol{U}_{sdq0}[K_{pc}(s-j\omega_g)+K_{ic}]}{\boldsymbol{I}_{sdq0}[K_{pc}(s-j\omega_g)+K_{ic}]} \\ Z_{\mathrm{DPC21}} \overset{middle\,f}{\approx} \dfrac{(s+j\omega_r-2j\omega_g)(s-j\omega_g)L_m\sigma+\boldsymbol{U}^{*}_{sdq0}[K_{pc}(s-j\omega_g)+K_{ic}]}{\boldsymbol{I}^{*}_{sdq0}[K_{pc}(s-j\omega_g)+K_{ic}]} \\ Z_{\mathrm{DPC22}} \overset{middle\,f}{\approx} \dfrac{(s+j\omega_r-2j\omega_g)(s-j\omega_g)L_m\sigma+\boldsymbol{U}^{*}_{sdq0}[K_{pc}(s-j\omega_g)+K_{ic}]}{(s+j\omega_r-2j\omega_g)(s-j\omega_g)\left[\dfrac{\sigma+1}{(s-2j\omega_g)}\right]} \end{cases} \tag{27}$$

It can be found that the DFIG system impedance based on DPC has four elements. For the sake of making some comparison with current control on the same Bode diagram, it entails the single-input single-output (SISO) transformation as shown in (28) [3].

$$Z_{\mathrm{SISO}}=\left[\frac{1}{Z_{11}}-\frac{Z_{gn}Z_{22}}{Z_{12}Z_{21}\left(Z_{22}+Z_{gn}\right)}\right]^{-1} \tag{28}$$

where, $Z_{gn}=(s-2j\omega_g)L_g$ denotes the negative-sequence grid impedance, and $L_g$ denotes the grid inductance. Then, the phase at 50 Hz for DPC can be calculated as (29), which is always -90° with unity power factor ($I_{sq0}=0$).

$$Z_{\mathrm{SISO\_DPC}}(j\omega_g)=\frac{-j\boldsymbol{U}_{sdq0}\boldsymbol{U}^{*}_{sdq0}}{\boldsymbol{I}_{sdq0}\boldsymbol{I}^{*}_{sdq0}\omega_g L_g} \tag{29}$$

Fig. 7 depicts the impedance Bode diagram of DFIG system for current control and DPC. The DFIG system has more sufficient phase margin when switching to DPC, since the intersection between DFIG system and grid (SCR=2) changes from 118 Hz to 91 Hz, and the phase difference decreases from 188° to 113°. The reason is that the phase at 50 Hz will increase from -180° to -90° after employing the DPC, resulting in the faster phase rise speed and narrower negative resistive region. And Fig. 8 validates that the DFIG system based on DPC also has sufficient phase margin under super-synchronous conditions.

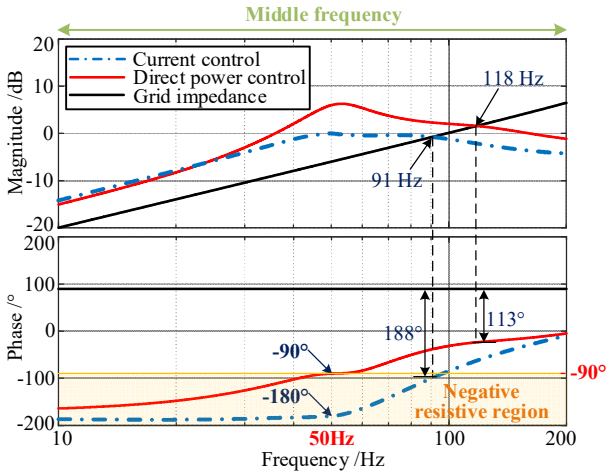


Fig. 7. Impedance Bode diagram of DFIG system for current control and direct power control within middle frequency.

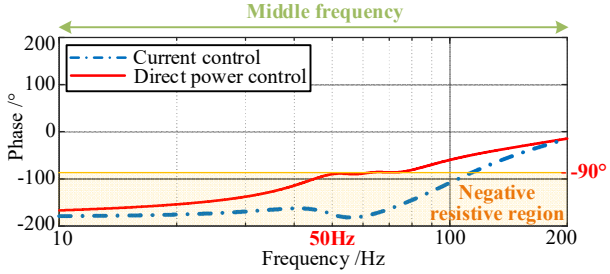


Fig. 8. Phase-frequency characteristic curves of DFIG system based on DPC under super-synchronous conditions ($f_r$= 60 Hz).

## B. *High-Frequency Negative Effect from DPC*

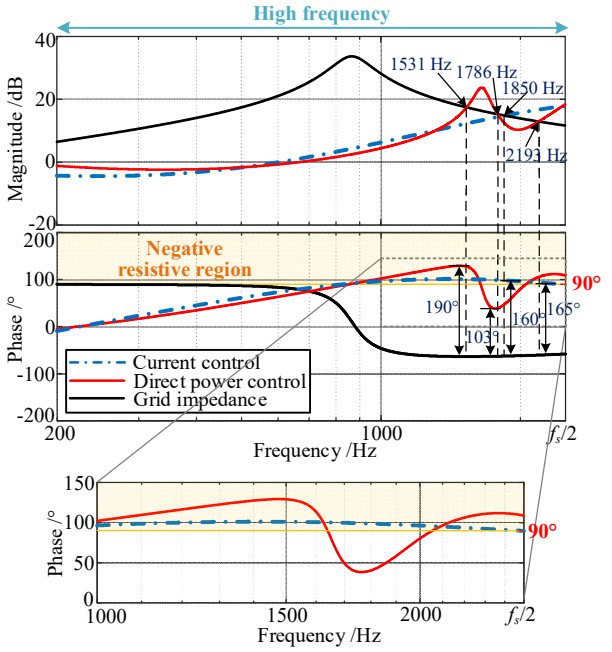


Fig. 9. Impedance Bode diagram of DFIG system for current control and direct power control at high frequency ($K_{pc}$=0.19, $K_{ic}$=19).

Even if the DPC can enhance the middle-frequency stability, it may cause some HFR when the grid parameters change. This

phenomenon is also observed in [22], but lacks some explanation.

According to Fig. 9, the DPC will produce more pronounced phase fluctuations and more obvious negative resistive characteristic at high frequency. Since the grid may include parallel compensation and long transmission cables, it will present high-frequency capacitive behavior [14]. When the grid parameters consist of series inductance $L_g$=0.51 mH, parallel capacitance $C_g$=0.067 mF and parallel resistance $R_g$=0.5 Ω, the amplitude–frequency characteristic curve for DPC will intersect the grid at 1531, 1786 and 2193 Hz, and the phase difference are 190°, 103° and 165°, respectively. Therefore, there is a potential instability risk at 1531 Hz for DPC.

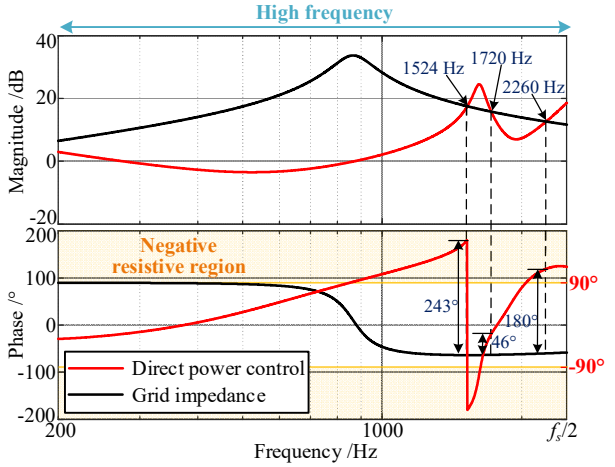


Fig. 10. Impedance Bode diagram of DFIG system for direct power control at high frequency ($K_{pc}$=0.26, $K_{ic}$=26).

When the PI gains of DPC increases to 0.26 and 26 in Fig. 10, this high-frequency negative resistive region will expand to -90° and -180°. There will be two potential risk frequency to aggravate instability, i.e. $f$=1524 Hz and $f$=2260 Hz.

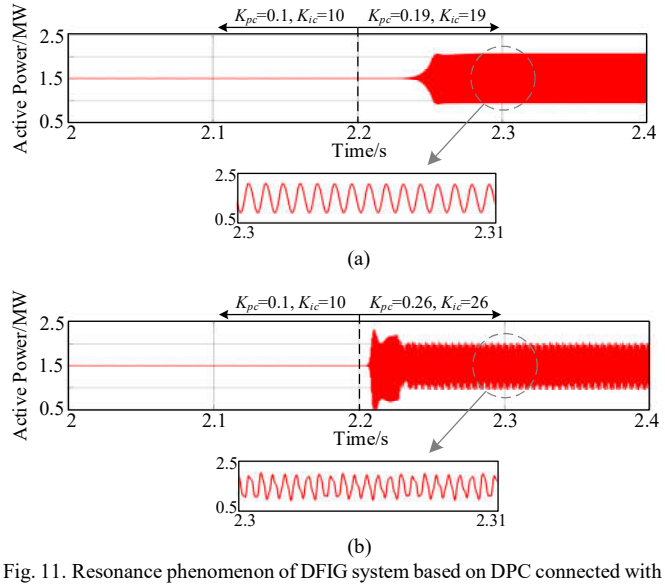


Fig. 11. Resonance phenomenon of DFIG system based on DPC connected with high-frequency capacitive grid ($L_g$=0.51mH, $C_g$=0.067mF, $R_g$=0.5Ω).

The simulation models of DFIG system connected with high-frequency capacitive grid are established in Matlab/Simulink. According to Fig. 11 (a), there are some HFR issues when the PI gains of power controller increases at 2.2 s. The number of resonance components further increases with larger PI gains as shown in Fig. 11 (b), i.e. $K_{pc}$=0.26 and $K_{ic}$=26, which is consistent with the conclusion of Fig. 10.

On the basis of fast Fourier transform (FFT) analysis in Fig. 12, the frequency coupling phenomenon is observed, indicating the additional resonance component that differs by 100 Hz when the DFIG-grid interconnected system oscillates. However, the frequency coupling characteristic is always related to the asymmetrical controller, and is attenuated at high frequency due to limited controller bandwidth [15].

Apart from that, there will be some deviations between Bode diagram and FFT results. It is caused by the output rotor voltage limitation or pulse width modulation (PWM) limitation, that can be corrected by some describing function [23]. Yet, this article pays more attention on the cause of this HFR rather than the accurate frequency prediction.

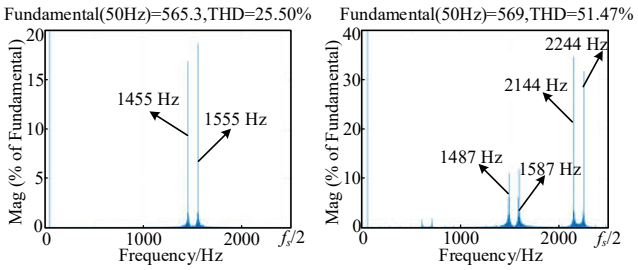


(a) $K_{pc}$=0.19, $K_{ic}$=19 (b) $K_{pc}$=0.26, $K_{ic}$=26

Fig. 12. FFT analysis of stator voltage.

To sum up, as a middle-frequency passivity enhancement method, the DPC presents the impedance reshaping band coupling. This phenomenon indicates that DPC can enhance the middle-frequency stability, but changes the impedance characteristics at high frequency, resulting in the bad performance under some complex grids, such as high-frequency capacitive grid.

### *C. Cause of Impedance Reshaping Band Coupling and Broadband Passivity Enhancement*

This subsection will analyze the cause of impedance reshaping band coupling and propose a broadband passivity enhancement method. As pointed out in Section IV.B, the system delay needs to be considered, the integral gain $K_{ic}$ is eliminated, and assuming $(s\text{-}j\omega_g)\approx s$ and $(s\text{-}j\omega_r)\approx s$ at high frequency. (27) can be rewritten as:

$$\begin{cases} Z_{\mathrm{DPC11}} = Z_{\mathrm{DPC22}} \overset{high\,f}{\approx} \dfrac{sL_m\sigma + \boldsymbol{U}_{sdq0}K_{pc}e^{-1.5s/f_s}}{\sigma+1} \\ Z_{\mathrm{DPC12}} = Z_{\mathrm{DPC21}} \overset{high\,f}{\approx} \dfrac{sL_m\sigma + \boldsymbol{U}_{sdq0}K_{pc}e^{-1.5s/f_s}}{\boldsymbol{I}_{sdq0}K_{pc}e^{-1.5s/f_s}} \end{cases} \tag{30}$$

For comparison with the current control in (16), the off-diagonal elements $Z_{\mathrm{DPC12}}$ and $Z_{\mathrm{DPC21}}$ are not zero at high frequency, indicating non-negligible frequency coupling. Besides, the $Z_{\mathrm{DPC11}}$, $Z_{\mathrm{DPC12}}$, $Z_{\mathrm{DPC21}}$ and $Z_{\mathrm{DPC22}}$ all contain the components of system delay $e^{-1.5s/fs}$, thus, the high-frequency

negative resistive characteristics from system delay is more prominent than current control.

Moreover, the numerator of $Z_{DPC11}$, $Z_{DPC12}$, $Z_{DPC21}$ and $Z_{DPC22}$ consists of $sL_m\sigma$ and system delay component $\boldsymbol{U}_{sdq0}K_{pc}e^{-1.5s/f_s}$, in which the magnitude of $sL_m\sigma$ will increase with larger $s$, while the magnitude of $e^{-1.5s/f_s}$ is always a constant. Therefore, as the frequency increases, the effect of system delay on numerator will be weakened.

However, as for the denominator of the off-diagonal elements $Z_{DPC12}$ and $Z_{DPC21}$, the system delay component $\boldsymbol{I}_{sdq0}K_{pc}e^{-1.5s/f_s}$ is not limited by $sL_m\sigma$. Thereby, the $Z_{DPC12}$ and $Z_{DPC21}$ pay the main responsibility to the pronounced phase fluctuations and intensify the negative resistive characteristics for DPC.

To circumvent this problem, it is expected while enhancing the stability within middle frequency, to avoid the high-frequency negative resistive characteristic from off-diagonal elements. According to (3), (4), (5), (7) and (26), only $\boldsymbol{G}_{PQi}$ has the off-diagonal elements. The basic idea is to introduce a low-pass filter in stator voltage to limit the high-frequency gain of $\boldsymbol{G}_{PQi}$. Fig. 13 demonstrates the DPC with a filter will not have the impedance reshaping band coupling and alleviate the risk of high-frequency instability. As long as the cut-off frequency of the low-pass filter is not too high, this phase fluctuation can be removed. While the phase fluctuation reappears when the cut-off frequency $f_{co}$=1500Hz. In addition, the cut-off frequency cannot be set too low to affect the dynamic response of fundamental frequency.

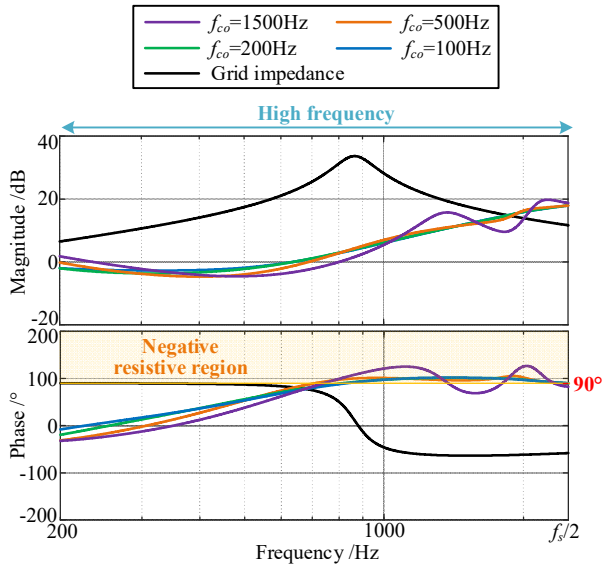


Fig. 13. Impedance Bode diagram of DFIG system for DPC with a filter at high frequency. ($K_{pc}$=0.26, $K_{ic}$=26)

Note that the other passivity enhancement methods within middle frequency may also affect the low or high frequency. The reason why this article chooses the DPC as a case study is that the DPC involves this interesting frequency coupling phenomenon. This broadband negative resistance analysis framework considering impedance reshaping band coupling can also be applied to some grid-forming control for DFIG middle-frequency stability enhancement, to avoid low-frequency resonance caused by series-compensated grid and drivetrain oscillation [24].

Note that the above analysis ignores the influence of GSC, while the GSC may influence the impedance characteristics with the extreme GSC parameter design. But the proposed DPC with filter in RSC is still effective, since the DFIG+RSC plays a leading role in introducing negative resistive characteristics.

### *D. Comparison with Existing Passivity Enhancement Method under Ultra-Weak Grid*

In addition to changing current control to direct power control to remove the Park transformation, [11] also proposes a virtual impedance (VI) that counteracts the negative effects of the Park transformation. However, the DPC has superiority under ultra-weak grid than the current control with VI.

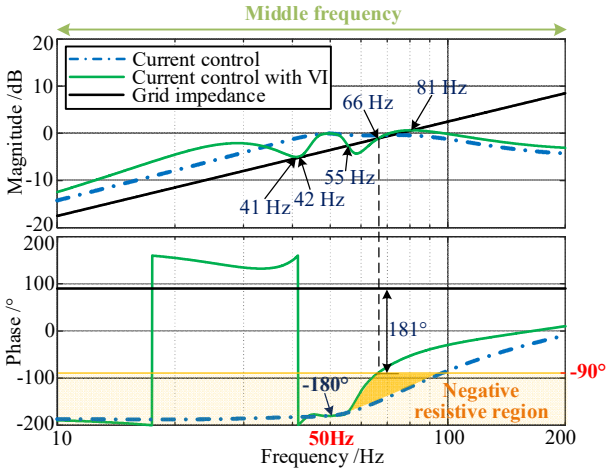


(a)

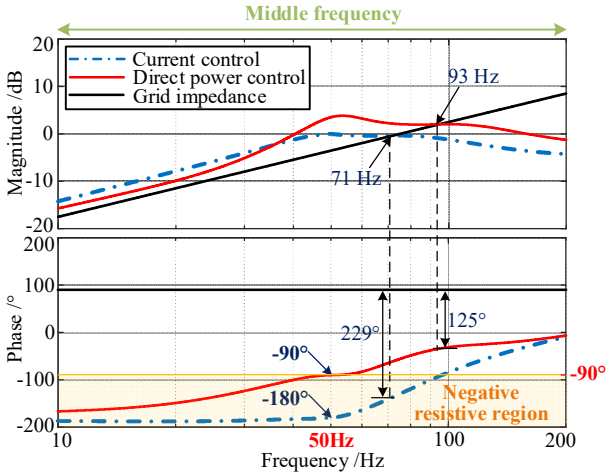


(b)

Fig. 14. Impedance Bode diagram of DFIG system for different passivity enhancement method under ultra-weak grid (SCR=1.5).

According to Fig. 14 (a), the high-pass filter of VI will inevitably reduce the magnitude of DFIG system around fundamental frequency, and the reshaped amplitude-frequency characteristic curve will intersect with the grid multiple times when the SCR=1.5. Since the negative impact of Park transformation only can be weakened while still existing, the phase at 50 Hz is still -180°. Therefore, when SCR decreases to 1.5 according to Fig. 14 (a), there are a lot of intersections such as 41Hz, 42 Hz, 55Hz, 66Hz and 81 Hz, of which 66 Hz is a

potential instability frequency bypassing (-1,0) in Nyquist diagram as shown in Fig. 15. However, the phase margin of DPC is more sufficient according to Fig. 14 (b), since the Park transformation is completely removed and the doesn't need a high-pass filter.

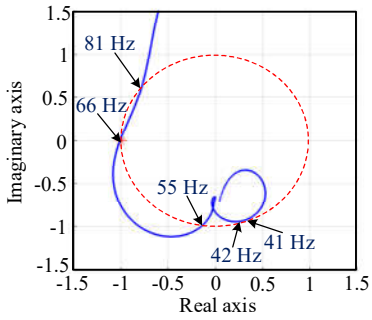


Fig. 15. Nyquist diagram of DFIG system for current control with virtual impedance (SCR=1.5).

## VI. Experimental Results

Fig. 16 depicts the hardware platform of control-hardware-in-loop (CHIL) experiment. The DFIG system model of 1.5 MW is developed in Typhoon 602+ with the time step of 1 μs. The control strategies are implemented in the TMS320F28335/Spartan6 XC6SLX16 DSP+FPGA control board. The parameters of DFIG system have been listed in Table I.


Fig. 16. Hardware platform of CHIL experiment.

This Section will compare the difference between the three control strategies as shown in Fig. 17, and validate the broadband passivity enhancement effect of DPC with filter.

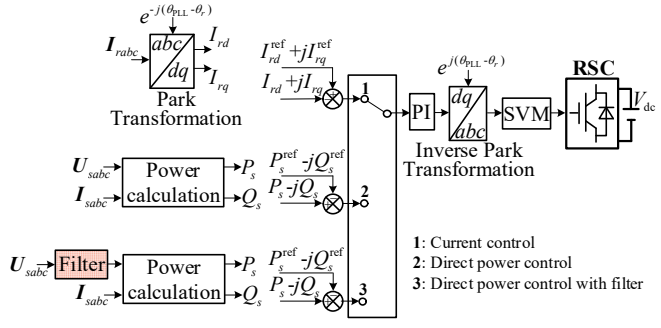


Fig. 17. Structure of three control strategy.

According to Fig. 18 and Fig. 19, when the PLL bandwidth $f_{bw\_PLL}$ increases from 50 Hz to 90 Hz, the DFIG-grid interconnected system subjects to the middle-frequency resonance issues under pure inductive grid or high-frequency capacitive grid. The resonant frequency at 91 Hz is the same as the analysis results in Fig. 7. When switching from current control to the DPC, the stability can be improved under pure inductive grid, while existing some HFR issues under high-frequency capacitive grid. The resonance frequency is 1455 and 1555 Hz, which has been predicted in the simulation of Fig. 12 (a). The total harmonic distortion (THD) of the stator voltage $\boldsymbol{U}_s$ and current $\boldsymbol{I}_s$ are 27.24% and 24.19%. The experimental results justify that the DFIG system based on DPC can enhance the middle-frequency phase margin. However, the DPC presents the impedance reshaping band coupling, which is vulnerable under some complex grids at high frequency, such as high-frequency capacitive grid.

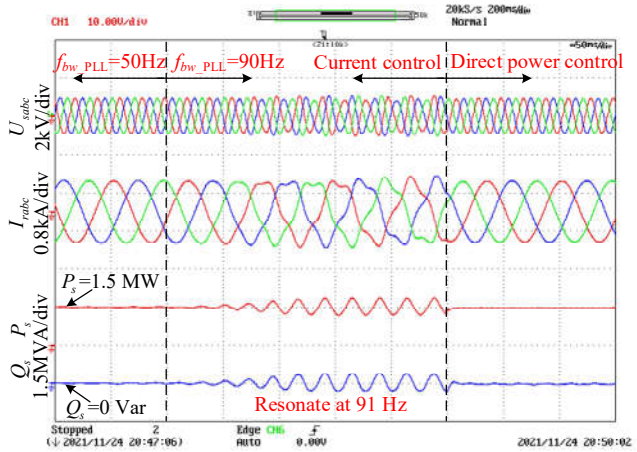


Fig. 18. Experimental results when switching from current control to direct power control under pure inductive grid ($L_g$=0.51mH).

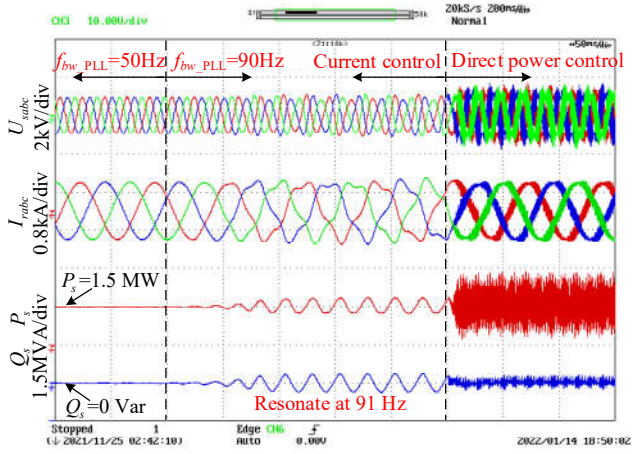


Fig. 19. Experimental results when switching from current control to direct power control under high-frequency capacitive grid ($L_g$=0.51mH, $C_g$=0.067mF, $R_g$=0.5Ω).

In order to realize the broadband passivity enhancement for DFIG system, a low-pass filter is enabled in stator voltage to counteract the high-frequency gain of $\boldsymbol{G}_{PQi}$. According to Fig. 20, when employing the proposed broadband passivity enhancement method, the high-frequency resonance is suppressed. The THD of the stator voltage $\boldsymbol{U}_s$ and current $\boldsymbol{I}_s$ are reduced to 0.95% and 0.92%.

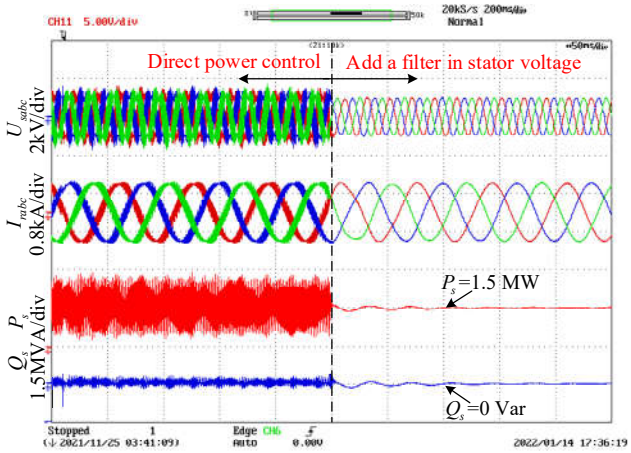


Fig. 20. Experimental results of the proposed broadband passivity enhancement method.

## VII. Conclusions

This article analyzes the impedance reshaping band coupling and broadband passivity enhancement for DFIG system. The answers to the three questions in Section I can be concluded as follows.

1) Compared with the GSC and dc-link dynamics, the control strategy of RSC plays a leading role in introducing negative resistive characteristics. When ignoring control, the DFIG system will behave as a negative resistor below the rotor frequency due to IGE. When considering control effect, there will be a broadband negative resistive region even if the rotor resistance is small.

2) This article proposes a unified form to express all the negative resistive mechanism. The reason of low-frequency negative resistive characteristic is SSCI, i.e. the proportional gain of current controller behaves as a low-frequency negative resistor. The middle-frequency negative resistive characteristic is related to the PLL, i.e. the phase of 50 Hz is restricted to -180° due to Park transformation. The high-frequency negative resistive characteristic is caused by system delay, i.e. the real part from $f_s/6$ to $f_s/2$ is negative.

3) DPC strategy can remove the negative resistive characteristic from Park transformation, and result in the faster phase rise speed and narrower negative resistive region within middle frequency. But when employing the DPC to enhance the phase margin within middle frequency, the impedance reshaping band coupling and pronounced high-frequency phase fluctuations are yielded. To this end, a low-pass filter is added in stator voltage to limit high-frequency frequency coupling and implement the broadband passivity enhancement effect.

## References


[1] Y. Qiu, S. Zhou, W. Gu, S. Ding, G. Han, K. Zhang and H. lv, "Multi-stage flexible planning of regional electricity-HCNG-integrated energy system considering gas pipeline retrofit and expansion," *IET Renew. Power Gener.*, vol. 16, no. 15, pp. 3339–3367, Aug. 2022.

[2] K. Liao, B. Pang, J. Yang and Z. He, "Compensation strategy of wideband voltage harmonics for doubly-fed induction generator," *IEEE Trans. Energy Convers.*, vol. 38, no. 1, pp. 674-684, Mar. 2023.

[3] C. Zhang, X. Cai, A. Rygg and M. Molinas, "Sequence domain SISO equivalent models of a grid-tied voltage source converter system for small-signal stability analysis," *IEEE Trans. Energy Convers.*, vol. 33, no. 2, pp. 741-749, Jun. 2018.

[4] Z. Yang, W. Liao, Q. Zhang, C. L. Bak and Z. Chen, "Fault coordination control for converter-interfaced sources compatible with distance protection during asymmetrical faults," *IEEE Trans. Ind. Electron.*, vol. 70, no. 7, pp. 6941-6952, Jul. 2023.

[5] R. Liu, J. Yao, X. Wang, P. Sun, J. Pei and J. Hu, "Dynamic stability analysis and improved LVRT schemes of DFIG-based wind turbines during a symmetrical fault in a weak grid," *IEEE Trans. Power Electron.*, vol. 35, no. 1, pp. 303-318, Jan. 2020.

[6] K. Sun, W. Yao, J. Fang, X. Ai, J. Wen and S. Cheng, "Impedance modeling and stability analysis of grid-connected DFIG-based wind farm with a VSC-HVDC," *IEEE J. Emerg. Sel. Topics Power Electron.*, vol. 8, no. 2, pp. 1375-1390, Jun. 2020.

[7] B. Hu, H. Nian, M. Li, Y. Xu, Y. Liao and J. Yang, "Impedance-based analysis and stability improvement of DFIG system within PLL bandwidth," *IEEE Trans. Ind. Electron.*, vol. 69, no. 6, pp. 5803-5814, Jun. 2022.

[8] J. Shair, X. Xie, J. Yang, J. Li and H. Li, "Adaptive damping control of subsynchronous oscillation in DFIG-based wind farms connected to series-compensated network," *IEEE Trans. Power. Del.*, vol. 37, no. 2, pp. 1036-1049, Apr. 2022.

[9] H. Liu, X. Xie, Y. Li, H. Liu and Y. Hu, "Mitigation of SSR by embedding subsynchronous notch filters into DFIG converter controllers," *IET Gener. Transmiss. Distrib.*, vol. 11, no. 11, pp. 2888-2896, Sep. 2017.

[10] A. E. Leon, "Integration of DFIG-based wind farms into series-compensated transmission systems," *IEEE Trans. Sustain. Energy.*, vol. 7, no. 2, pp. 451-460, Apr. 2016.

[11] H. Nian, B. Hu, Y. Xu, C. Wu, L. Chen and F. Blaabjerg, "Analysis and reshaping on impedance characteristic of DFIG system based on symmetrical PLL," *IEEE Trans. Power Electron.*, vol. 35, no. 11, pp. 11720-11730, Nov. 2020.

[12] B. Hu, H. Nian, M. Li, Y. Liao, J. Yang and H. Tong, "Impedance characteristic analysis and stability improvement method for DFIG system within PLL bandwidth based on different reference frames," *IEEE Trans. Ind. Electron.*, vol. 70, no. 1, pp. 532-543, Jan. 2023.

[13] I. Vieto, and J. Sun, "Sequence impedance modeling and analysis of type-III wind turbines", *IEEE Trans. Energy Convers.*, vol. 33, no. 2, pp. 537-545, Jun. 2018.

[14] H. Nian and B. Pang, "Stability and power quality enhancement strategy for DFIG system connected to harmonic grid with parallel compensation," *IEEE Trans. Energy Convers.*, vol. 34, no. 2, pp. 1010-1022, Jun. 2019.

[15] H. Wu and X. Wang, "Virtual-flux-based passivation of current control for grid-connected VSCs," *IEEE Trans. Power Electron.*, vol. 35, no. 12, pp. 12673-12677, Dec. 2020.

[16] X. Wang, Y. He, D. Pan, H. Zhang, Y. Ma and X. Ruan, "Passivity enhancement for LCL-filtered inverter with grid current control and capacitor current active damping," *IEEE Trans. Power Electron.*, vol. 37, no. 4, pp. 3801-3812, Apr. 2022.

[17] L. Harnefors, X. Wang, A. G. Yepes and F. Blaabjerg, "Passivity-based stability assessment of grid-connected VSCs—An overview," *IEEE J. Emerg. Sel. Topics Power Electron.*, vol. 4, no. 1, pp. 116-125, Mar. 2016.

[18] H. Nian, Y. Liu, H. Li, B. Hu, Y. Liao and J. Yang, "Commutation overlap characteristic modeling and stability analysis of LCC-HVDC in sending AC grid," *IEEE Trans. Sustain. Energy.*, vol. 13, no. 3, pp. 1594-1606, Jul. 2022.

[19] T. Xue, J. Lyu, H. Wang and X. Cai, "A complete impedance model of a PMSG-based wind energy conversion system and its effect on the stability analysis of MMC-HVDC connected offshore wind farms," *IEEE Trans. Energy Convers.*, vol. 36, no. 4, pp. 3449-3461, Dec. 2021.

[20] L. Wang, X. Xie, Q. Jiang, H. Liu, Y. Li and H. Liu, "Investigation of SSR in practical DFIG-based wind farms connected to a series-compensated power system," *IEEE Trans. Power Syst.*, vol. 30, no. 5, pp. 2772-2779, Sep. 2015.

[21] Z. Gong, C. Liu, L. Shang, Q. Lai and Y. Terriche, "Power decoupling strategy for voltage modulated direct power control of voltage source inverters connected to weak grids," *IEEE Trans. Sustain. Energy.*, vol. 14, no. 1, pp. 152-167, Jan. 2023.

[22] Z. Xie, W. Wu, Y. Chen and W. Gong, "Admittance-based stability comparative analysis of grid-connected inverters with direct power control and closed-loop current control," *IEEE Trans. Ind. Electron.*, vol. 68, no. 9, pp. 8333-8344, Sep. 2021.

[23] S. Shah and L. Parsa, "Impedance-based prediction of distortions generated by resonance in grid-connected converters," *IEEE Trans. Energy Convers.*, vol. 34, no. 3, pp. 1264-1275, Sep. 2019.
[24] L. Chen, X. Du, B. Hu and F. Blaabjerg, "Drivetrain oscillation analysis of grid forming type-IV wind turbine," *IEEE Trans. Energy Convers.*, vol. 37, no. 4, pp. 2321-2337, Dec. 2022.

**Bin Hu** (S'21) was born in Wenzhou, China. He received the B.Eng. degree in electrical engineering from Shenyang University of Technology, Shenyang, China, in 2018. He is currently working towards the Ph.D. degree of electrical engineering in Zhejiang University.

He has worked as a Visiting Student with the Department of Energy Technology, Aalborg University, Aalborg, Denmark, from 2021 to 2022. His research interests include large-signal and small-signal synchronization stability of converter-based resources, especially doubly fed induction generator (DFIG)-based wind power systems.

Mr. Hu was a recipient of the Best Paper Award of IEEE TRANSACTIONS ON ENERGY CONVERSION in 2022.

**Heng Nian** (M'09–SM'14) received the B.Eng. and M.Eng. degrees in electrical engineering from the Hefei University of Technology, Hefei, China, in 1999 and 2002, respectively, and the Ph.D. degree in electrical engineering from Zhejiang University, Hangzhou, China, in 2005.

From 2005 to 2007, he was a Postdoctoral Researcher with the College of Electrical Engineering, Zhejiang University, where he became an Associate Professor in 2007 and has been a Full Professor of electrical engineering since 2016. From 2013 to 2014, he was a Visiting Scholar with the Department of Electrical, Computer, and System Engineering, Rensselaer Polytechnic Institute, Troy, NY, USA.

He has published more than 40 IEEE/IET Transaction papers and holds more than 20 issued/pending patents. His current research interests include optimal design and operation control for wind power generation systems.

**Haipan Li** was born in Shanxi, China. He received the B.Eng. degree from Zhejiang University, Hangzhou, China, in 2020. He is currently working toward the Ph.D. degree of electrical engineering in Zhejiang University, Hangzhou, China.

His research interests include small-signal modeling of renewable generators, their integration to the electric grid and system stability analysis.

**Liang Chen** received the B.Eng. and Ph.D. degrees in electrical engineering from Zhejiang University, Hangzhou, China, in 2014, and 2020, respectively.

From 2020 to 2022, he was a Postdoctoral Researcher with the Department of Energy Technology, Aalborg University, Aalborg, Denmark. He is currently an Assistant Professor with the School of Information Science and Engineering, NingboTech University, Ningbo, China. His research interests include modeling of integration of renewable energy to the grid and corresponding stability analysis.

**Subham Sahoo** (S'16-M'18-SM'23) received the B.Tech. & Ph.D. degree in Electrical and Electronics Engineering from VSSUT, Burla, India and Electrical Engineering at Indian Institute of Technology, Delhi, New Delhi, India in 2014 & 2018, respectively. He is currently an Assistant Professor in the Department of Energy, Aalborg University (AAU), Denmark, where he is also the vice-leader of the research group on Reliability of Power Electronic Converters (ReliaPEC) in AAU Energy.

He is a recipient of the Indian National Academy of Engineering (INAE) Innovative Students Project Award for the best PhD thesis across all the institutes in India for the year 2019. He is selected into EU-US National Academy of Engineering (NAE) Frontier of Engineering (FOE) Class of 2021. He was also a distinguished reviewer for IEEE Transactions on Smart Grid in 2020. He is currently the vice-chair of IEEE PELS Technical Committee (TC) 10 on Design Methodologies. He was the secretary of the IEEE YP Affinity Group, Denmark in 2020-2022. He is an Associate Editor on IEEE Transactions on Transportation Electrification.

His research interests are control, optimization, cybersecurity and stability of power electronic dominated grids, application of artificial intelligence and machine learning in power electronic systems.

**Frede Blaabjerg** (S'86–M'88–SM'97–F'03) was with ABB-Scandia, Randers, Denmark, from 1987 to 1988. From 1988 to 1992, he got a Ph.D. degree in Electrical Engineering at Aalborg University in 1995. He became an Assistant Professor in 1992, an Associate Professor in 1996, and a Full Professor of power electronics and drives in 1998. From 2017 he became a Villum Investigator. He is honoris causa at University Politehnica Timisoara (UPT), Romania, and Tallinn Technical University (TTU) in Estonia. His current research interests include power electronics and its applications, such as in wind turbines, PV systems, reliability, harmonics, and adjustable speed drives. He has published more than 600 journal papers in the fields of power electronics and its applications. He is the co-author of four monographs and editor of ten books in power electronics and its applications.

He has received 32 IEEE Prize Paper Awards, the IEEE PELS Distinguished Service Award in 2009, the EPE-PEMC Council Award in 2010, the IEEE William E. Newell Power Electronics Award 2014, the Villum Kann Rasmussen Research Award 2014, the Global Energy uPrize in 2019 and the 2020 IEEE Edison Medal. He was the Editor-in-Chief of the IEEE TRANSACTIONS ON POWER ELECTRONICS from 2006 to 2012. He has been a Distinguished Lecturer for the IEEE Power Electronics Society from 2005 to 2007 and for the IEEE Industry Applications Society from 2010 to 2011 as well as 2017 to 2018. In 2019-2020 he served a President of the IEEE Power Electronics Society. He is Vice-President of the Danish Academy of Technical Sciences too. He is nominated in 2014-2019 by Thomson Reuters to be between the most 250 cited researchers in Engineering in the world.